Building memristive and radiation hardness TiO$_2$-based junctions

N. Ghenzi [a,*], D. Rubi [a,b,c], E. Mangano [d], G. Gimenez [d], J. Lell [a], A. Zelcer [b,e], P. Stoliar [b,f], P. Levy [a,c]

[a] Gerencia de Investigación y Aplicaciones, Comisión Nacional de Energía Atómica, Argentina
[b] ECyT, UNSAM, Martín de Irigoyen 3100, 1650 San Martín, Bs As, Argentina
[c] Consejo Nacional de Investigaciones Científicas y Técnicas (CONICET), Argentina
[d] Instituto Nacional de Tecnología Industrial (INTI), Argentina
[e] Gerencia Química, Comisión Nacional de Energía Atómica, Argentina
[f] IMN, Université de Nantes, CNRS, 2 rue de la Houssinière, BP 32229, 44322 Nantes, France

ARTICLE INFO

ABSTRACT

We study micro-scale TiO$_2$ junctions that are suitable to be used as resistive random-access memory nonvolatile devices with radiation hardness memristive properties. The fabrication and structural and electrical characterization of the junctions are presented. We obtained a retentivity of 10^5 s, an endurance of 10^4 cycles and reliable switching with short electrical pulses (time-width below 10 ns). Additionally, the devices were exposed to 25 MeV oxygen ions. Then, we performed electrical measurements comparing pristine and irradiated devices in order to check the feasibility of using these junctions as memory elements with memristive and radiation hardness properties.

© 2013 Elsevier B.V. All rights reserved.

1. Introduction

A variety of metal-oxide interfaces exhibit reversible and non-volatile changes between two stable electric resistance states after the application of pulsed electric stimulus (voltage or current). Intense basic research [1–3] focuses on this electric pulse induced resistive switching (RS) effect as a candidate for memory devices because it allows downscaling and exhibits high retentivity time, multilevel states and low power consumption. Besides, this emerging technology, called resistive random-access memory (RRAM), exhibits fast switching speeds (<ns [4]) and high endurance, characteristics that turn it into a good candidate to compete with existing flash memory devices.

Resistive switching is found in both binary and complex oxides. Memory cells based on binary oxides have a rather simple structure and composition when compared with (perovskite-like) complex-oxide-based cells. In addition, they present high compatibility with complementary metal oxide semiconductor processes and retention times of more than 10^6 s [2]. A large variety of binary oxides have been explored for RRAM applications, such as NiO [5], ZnO [6], WO [7], HfO$_2$ [8–10], CuO [11], and TiO$_2$ [12], among others.

Recently, titanium dioxide captured significant attention as it exhibits robust RS properties [3]. After an initial electroforming process, the electrical conduction in TiO$_2$-based metal–insulator–metal (MIM) structures can be controlled by spatially heterogeneous barriers,

i.e. filaments, as in many other binary oxides. These filaments are formed by ionic defects like oxygen vacancies or interstitial metal cations.

Presently, flash is the widely used technology for memory devices in aerospace and nuclear industry, which requires radiation hardness characteristics. This technology offers high storage density and immunity to power failure. However, their large programming voltage requires an external charge pump that is prone to fail under radiation conditions [13]. Non-volatile memories relying on the RS effect are based on the change of a physical property of the junction instead of charge storage. The resistance change mechanism is supposed to have enough radiation hardness to justify its use in aerospace and nuclear applications and in other critical environments as well [14–17].

In this work we describe the fabrication and characterization of MIM junctions showing memristive properties, foreseeing their use as radiation hardness non-volatile memory devices.

2. Experimental details

We studied TiO$_2$-based MIM junctions with metal electrodes of Au, Al and Cu. The area of the devices ranged between 2 μm × 2 μm and 500 μm × 500 μm in a crossbar pattern. Titanium dioxide thin layers were prepared by reactive R.F. sputtering (13.56 MHz) from a metallic Ti target (purity 99.98%, diameter 8 cm). The sputtering chamber was initially evacuated to a base pressure of 10^{-5} Pa. Deposition was performed in an O$_2$/Ar mixture (total pressure 2.7 Pa) at room temperature. The oxygen partial pressure was optimized to obtain the stoichiometric oxide. The substrates were rotated during deposition in order to obtain homogeneous films. The target–substrate distance was

fixed at 8.9 cm. Typically, we deposited 50 nm thick layers. The metallic top electrode (TE) and the bottom electrode (BE) were made by thermal evaporation method. The crossbar pattern was obtained by using standard lift off processes that defined each of the three layers (BE = Au, dielectric = TiO_2 and TE = Al, Cu and Au).

Both the optical constants and the thickness of the films were extracted from ellipsometry measurement (Gaertner ellipsometer, He–Ne laser). AFM images were performed by the stand-alone SMENA NTMDT microscope in semi-contact mode in air using silicon tips (NSG01, NT-MDT) with typical resonant frequency 150 kHz and force constant 5.5 N/m. The roughness analysis mode of images was analyzed using the software NOVA v.1.0.26.874 (NT-MDT) which calculates the basic statistical parameters for the source object (2D function) and forms the function value distribution density histogram. Root mean square (RMS) roughness is in accordance with ISO 4287/1.

The electrical characterization (pulsed current–voltage I–V curves and remnant hysteresis switching loops, HSL) was performed with a source-measurement unit Keithley 2400 hooked to a probe station. Data was acquired using custom software (LabVIEW environment). Nanosecond voltage pulses were produced by an Agilent 8110A pulse generator. We measured the remnant resistance between pulses by applying a small constant bias voltage $V_{read} = 0.1$ V, *i.e.*, the read operation of the memory device. Our crossbar of MIM junctions operates with electrical pulses ranging from 10^6 to 10^7 V/cm. These electric fields, which are available in standard portable electronic appliances, are of the order of the dielectric breakdown field of the insulator ($3 \cdot 10^6$ V/cm) [18].

3. Results

Fig. 1(a–b) displays the ellipsometry parameters $tan(\Psi)$ and $cos(\Delta)$, defined by the ratio $\rho = tan(\Psi)exp(i\Delta)$, as a function of the wavelength for an unpatterned TiO_2 sample. The experimental data were fitted with the Forouhi–Bloomer model for dielectrics [19] using the optical constants of TiO_2. We obtained a good agreement between this isotropic model and the experimental data for O_2/Ar ratio (in pressure) above 1/3, indicating that this is the mixture gas ratio threshold for the oxide formation (otherwise the film remains metallic). Typically, the film thickness reported by the fitting procedure was 47 nm. The good fit obtained by using an isotropic model, together with X-ray diffraction (XRD) measurements (not shown here), suggests that the films present a low degree of crystallinity.

In Fig. 1(c) we show a scanning electron microscopy (SEM) image of a TiO_2 film. The SEM image was recorded with 3 kV electrons and an amplification of ×500,000. The surface exhibits a granular structure with a grain size around 70 ± 20 nm. The non-contact atomic force microscopy (AFM) image of Fig. 1(d) is in agreement with the results of SEM analysis. AFM image analysis indicates a root mean square (RMS) roughness of ~4.78 nm. The combination of ellipsometry, XRD and microscopy data suggests that our film microstructure is compatible with a network of poorly crystallized nanograins.

Fig. 2(a) shows a typical crossbar structure consisting of six junctions with their corresponding electrodes. In this image, the BE (vertical) is 50 nm thick and 100 μm wide, while the TE (horizontal) is 50 nm thick and 25 μm wide. Fig. 2(b) presents a cross-section of one
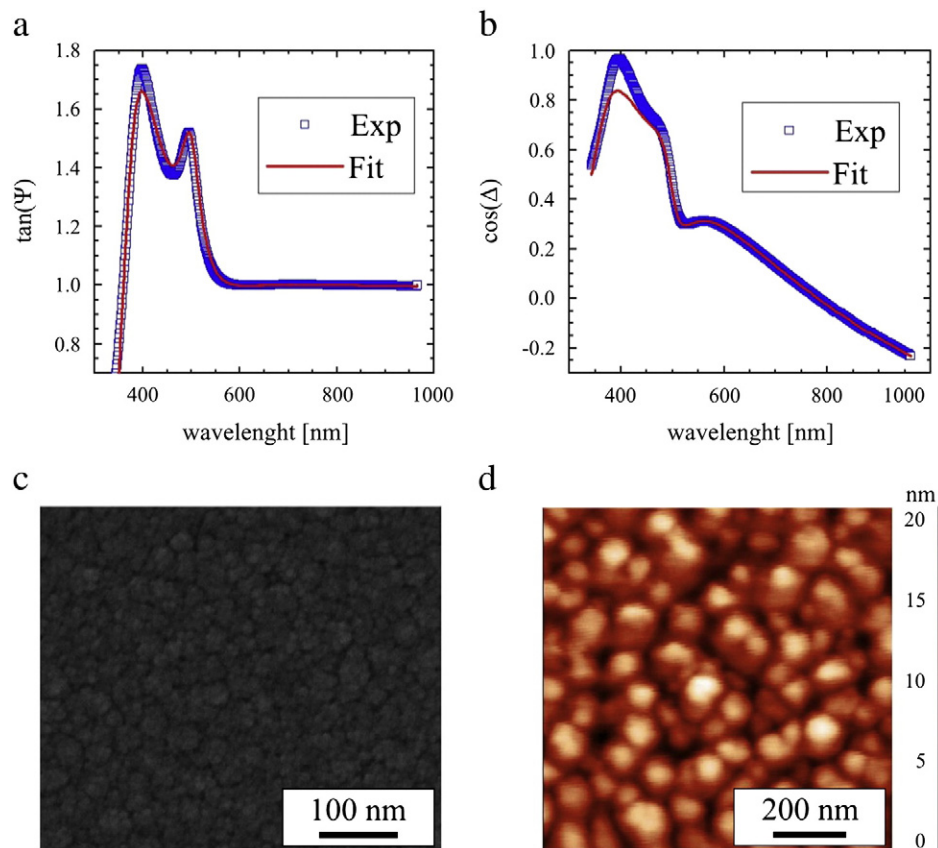
Fig. 1. Ellipsometry measurements ((a) amplitude and (b) phase) of an unpatterned 47 nm-thick TiO_2 sample. (c) Scanning electron microscopy and (d) atomic force microscopy images of the same sample.
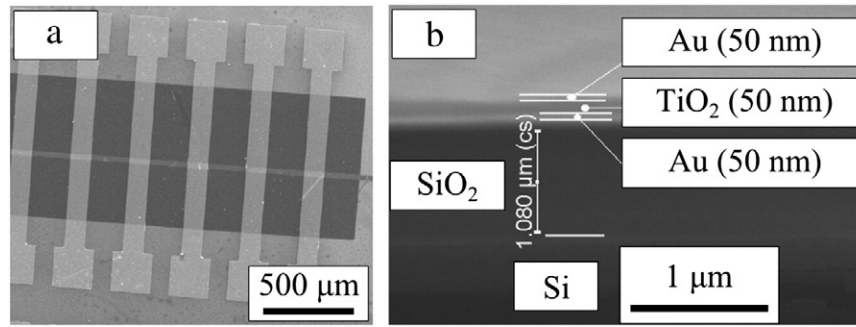
Fig. 2. (a) SEM image of the crossbar array consisting of 6 junctions. (b) Cross-section of the trilayer 50 nm Au/50 nm TiO₂/50 nm Au performed with a focused ion beam.

of the MIM devices obtained by focused ion beam (FIB). The MIM trilayer (50 nm Au/50 nm TiO$_2$/50 nm Au) can be clearly seen on top of the Si substrate with the 1 μm-thick SiO$_2$ thermal oxide layer. The SEM images were recorded with 15 kV electrons and an amplification of ×160 (Fig. 2(a)) and ×93,000 (Fig. 2(b)) with a Everhart–Thornley detector.

Now we focus on the RS properties. It is worth remarking that there are several key issues that are not completely elucidated regarding the RS mechanism. The first one has to do with the role of defects such as oxygen vacancies or metal ions percolating in the oxide matrix. In addition, the role of the interface between the metal electrode and the oxide film, which controls the amount of electric carriers injected into the dielectric, is very important. It is believed that the contact between the metal and the oxide plays a crucial role in the resistance change as, depending on the properties of the metal, it might present an ohmic contact, a Schottky barrier or a naturally grown metal oxide layer.

Another issue is related to the nature of the metal electrodes. We recall that even if Pt has been widely used for contacting TiO$_2$ due to its robustness [3], we used Au, Al and Cu as metal electrodes. Au has a similar work function to that of Pt ([20]); therefore it would probably form a Schottky barrier as well. Upon appropriate processes, Al is expected to form a native oxide layer of Al$_2$O, which might improve the reproducibility of the RS properties among devices [21]. In the case of devices with Cu electrode, two hypotheses can be drawn; either Cu+ could migrate during electroforming producing a solid metal filament bridging the two electrodes, or vacancies could generate a conductive sub-oxide filament as well. As we shall later see, the switching process occurring at negative polarity rules out the Cu+ migration, indicating that oxygen vacancies are the predominant defect in the oxide.

The asymmetric electrode structure we have chosen allows comparing the forming voltage and the leakage current related to the different

top electrodes. All the other components of the MIM structures remain identical.

Fig. 3(a) depicts the setup used for the electrical measurements. Voltage was applied to the TE while the BE was grounded. Next we discuss the initialization process, *i.e.* the electroforming of the pristine devices, with three different materials as top electrode TE (Cu, Au and Al) and Au as a BE.

Forming in the explored samples was obtained with negative voltages. After the forming the device remains in the OFF state. When positive electroforming was tested, we did not observe an increase of the current up to 20 V or unstable RS behavior. Therefore we focused exclusively on the negative polarity electroforming, which renders stable RS properties [22].

Negative electroforming (F−) consisted in slowly increasing the voltage, as shown in Fig. 3(b), until a transition to a lower resistance state than the virgin state was found, evidencing the initialization of the conduction process. The current limit (compliance) of the source-meter avoided damaging the device during this abrupt initialization process.

The low currents observed at low bias evidence the insulating capabilities of the titanium dioxide in all the TE configurations. However, the three electrodes presented different electroforming voltages: −3 V for Cu, −5.8 V for Au and −8 V for Al. This difference might rely on the different work functions of each metal. The corresponding leakage currents at 2 V were 10 μA, 1 μA and 10 nA, respectively. We also found a significant correlation between the leakage currents and the forming voltage, *i.e.*, the higher the leakage current, the lower the forming voltage.

After the electroforming process shown in Fig. 3(b), we studied the effect of applying further bipolar electrical pulses. Indeed, we applied voltage pulses with a sequence 0 V → 3 V → −3 V → 0 V in steps of
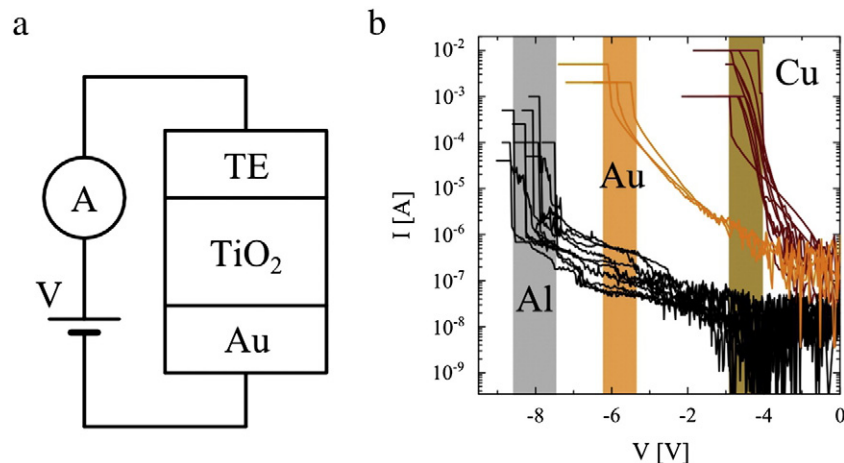
Fig. 3. (a) Schematic diagram of the experimental setup. The bottom electrode is always connected to ground. (b) Initialization process of junctions showing the different behaviors for Cu, Al and Au top electrodes. We found forming voltages of −3 V for Cu, −5.8 V for Au and −8 V for Al, while the leakage current at 2 V is 10 μA, 1 μA and 10 nA respectively.

0.1 V. The compliance current was kept at 10 mA to prevent damage in the devices. A delay of 1 s was inserted between pulses to limit the Joule heating. The measurement of the remnant resistance was carried out during these intervals. Here we present measurements for Al (50 nm)/TiO$_2$ (50 nm)/Au (50 nm). Results for the other TE are qualitatively similar; they will be reported elsewhere.

Remarkably, we observed a typical bipolar switching behavior as shown in Fig. 4(a). Initially, the device was in the high resistance (HR) state. When a voltage of +1 V (SET or ON transition) was reached, the device switched to the low resistance (LR) state. After changing the polarity, the device switched back to HR (RESET or OFF transition) for voltage exceeding −2 V. The non-linear behavior of the LR state indicates that the device was operating in bipolar resistive switching mode.

In the same run, between two consecutive pulses, we measured the remnant (two terminals) resistance using small bias (0.1 V). Fig. 4(b) plots the obtained HSL in which the voltage of the SET and RESET transitions coincides with the observations at the I–V curves [23]. The remnant resistance exhibits two well-defined resistance states (*i.e.*, a HR state of approximately 60 Ω and a HR state that reaches 500 Ω) and two abrupt transitions (*i.e.*, SET and RESET).

Fig. 4(c) presents the evolution of the V$_{SET}$ and V$_{RESET}$ during 500 cycles that is qualitatively similar to that shown in Fig. 4(b). This analysis, performed on 10 different devices, evidences low dispersion as well as a rather stable behavior (see Fig. 4(d)). Among devices, there is a correlation between the V$_{SET}$ and V$_{RESET}$; if one of the threshold voltages decreases the other follows its trend. This effect might be related to the specific structure of filaments at each junction.

Fig. 5(a) shows the retentivity of the HR and LR states at room temperature. For this analysis, we measured repetitively the remnant state of a junction after setting it to the HR state (*i.e.* a read current of 90 μA

at 0.1 V bias). We observed a decrease of only 10 μA (*i.e.*, 10% decay) after 10^5 s. Then, we repeated the measurement for the LR state (*i.e.*, 692 μA at 0.1 V bias). In this case, the drift in the reading current was 16 μA after 10^5 s, that is, a decrease of 0.02%.

When cycling, a net drift of oxygen vacancies away from the TiO$_2$–Au interface is produced due to the higher electric field in the interface. This drift results in the requirement of a sustained increase of the voltage pulses in order to achieve resistive switching [24]. The LRS defect distribution is smoother than that corresponding to the HRS, which produces a higher stability, and then a better retention property [23].

In order to explore the maximum number of cycles the devices can undergo while keeping a significant gap between HR and LR, we tested a cell by applying alternated negative/positive pulses (±3 V, 1 ms). Between these pulses, a bias voltage of 0.1 V was applied to measure the resistance state. The result of this endurance test is presented in Fig. 5(b). We reached 10^4 cycles without having any important reduction of the gap between the two states. Further pulsing resulted in an overlap of the HR and LR levels, blurring the gap between them.

These measurements are a clear proof that our devices can be used as a non-volatile memory, provided that their "use-life" is limited in the number of switching events. In addition, by including an "intelligent" pulsing strategy [24,25] this degradation can be significantly reduced, as it is mainly consequence of unbalanced accumulation of oxygen vacancies.

The switching characteristics of these devices as a function of the width of the pulses used for the ON transition were also tested. We explored the range between 10 ns and 1 μs, while the OFF transition was always accomplished with pulses of 100 ns. In order to safely ensure the ON switching, a voltage of 3 V was used in these experiments, that is, 3 times higher than the SET voltage reported in Fig. 4(b) where pulses
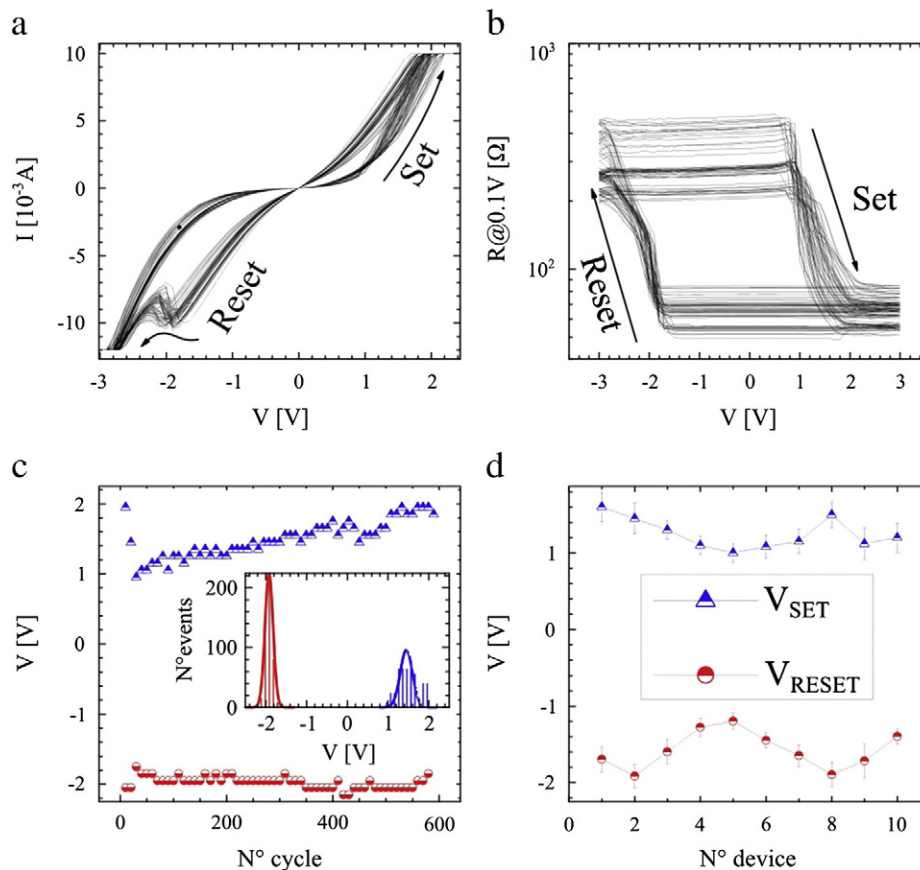
Fig. 4. (a) Current–voltage I–V and (b) HSL curves of Al (50 nm)/TiO$_2$ (50 nm)/Au (50 nm) junctions. The compliance of the instrument (I$_{cc}$) was set to 10 mA. (c) V$_{SET}$ and V$_{RESET}$ as a function of the cycle number. Inset: histograms of V$_{SET}$ and V$_{SET}$. (d) V$_{SET}$ and V$_{RESET}$ for 10 different junctions; each data point represents the average and standard deviation obtained from Gaussian fits, as presented in the inset of (c).
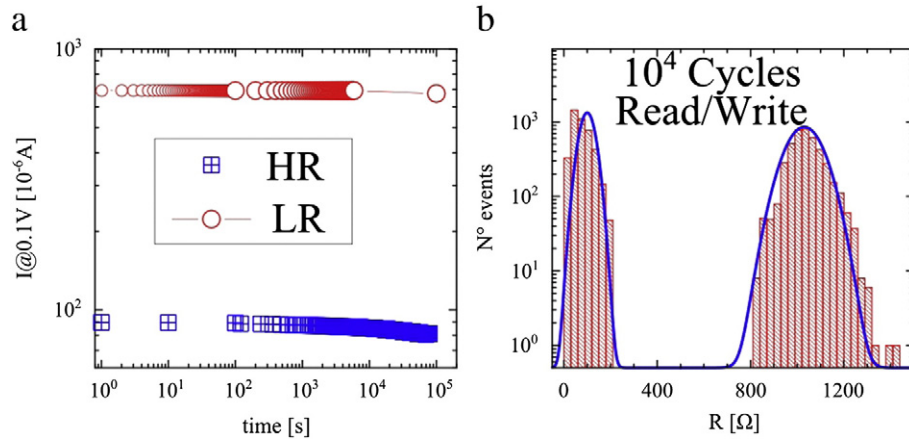
Fig. 5. (a) Retentivity of HR and LR states of a Al/TiO$_2$/Au memory cell at room temperature; (b) endurance test on a Al/TiO$_2$/Au memory cell at room temperature (see Section 3).

were 1 ms-width. Results are shown in Fig. 6(a). In all cases we obtained an ON transition, yet the ON/OFF ratio was higher for longer pulses. We hypothesize that when the voltage is applied during longer times, more conductive filaments appear or bigger filaments grow inside the oxide. This effect is related in a similar way to the fact that higher applied current produces lower LRS [2].

In order to test the radiation hardness of our devices, we chose to irradiate them with ions instead of gamma rays. Basically, the stopping power of heavy ions (the amount of energy deposited per unit distance) increases as the ions slow down. Indeed, the so called "Bragg peak", which indicates the position where the maximum energy is deposited, occurs at the end of the trajectory of the ion. In contrast, the energy deposition from a photon beam decays exponentially with the traveled distance. Thus, ion radiation produces a relatively higher damage inside the oxide film. We used this tool as a way to introduce controlled damage to our devices. Oxygen was selected as the beam ion as it was the ion with heavier atomic weight available and it should therefore maximize the irradiation damage on the devices. We exposed them to high-energy oxygen ions. 200 devices were introduced in an irradiation (vacuum) chamber at Tandar electrostatic accelerator [26] where 100 of them were irradiated with ^{16}O at 25 MeV. The ionization state of the ions was 5 +. The remaining devices were shielded and used as blank, *i.e.*, they were exposed to the same atmospheric conditions and electrical testing protocol, but not to the ions. The beam was defocused with a magnetic lens to ensure a uniform dose distribution throughout the

devices. We used an array of 9 Faraday cups (*i.e.*, instrument to measure the ion flux) to check the uniformity and to measure the dose applied to the devices [27], that was fixed to 10^{12} ions/cm^2. Note that 25 MeV is not enough energy for oxygen ions to produce nuclear reactions so that the devices do not become radioactive after the irradiation, which would produce mistakes in the dosimetry if the sample keeps self-irradiating [28]. The ions arrived to the devices perpendicular to the top electrode, depositing/losing energy mainly through electronic collisions.

At 25 MeV, oxygen ions deposited 85 keV in the aluminum TE, 125 keV in the dielectric layer, 230 keV in the BE, and finally they penetrated ~17 µm into the substrate. We calculated these values with the SRIM software [29]. Due to the initial energy of the ions, the energy deposition in these 3 first layers is almost uniform (in the direction the ions advanced) across each one. The ions stopped well inside the substrate so that they do not remain as oxygen doping in the active layer. In fact, each oxygen ion left in the TiO$_2$ layer has a linear trail of electronic defects that resulted from the transfer of 125 keV out of its kinetic energy. Ions generated a total of 2.5 · 10^8 columnar defects in each device while traveling through this dielectric layer [30].

We recall that the total ion dose is not high enough to expect macroscopic effects. On the other hand, such dose rate can indeed produce a significant change in the filament formation mechanisms during the electroforming process. Thus, after irradiation, we evaluated the electroforming characteristics of both batches (*i.e.*, the irradiated devices and the blank samples).
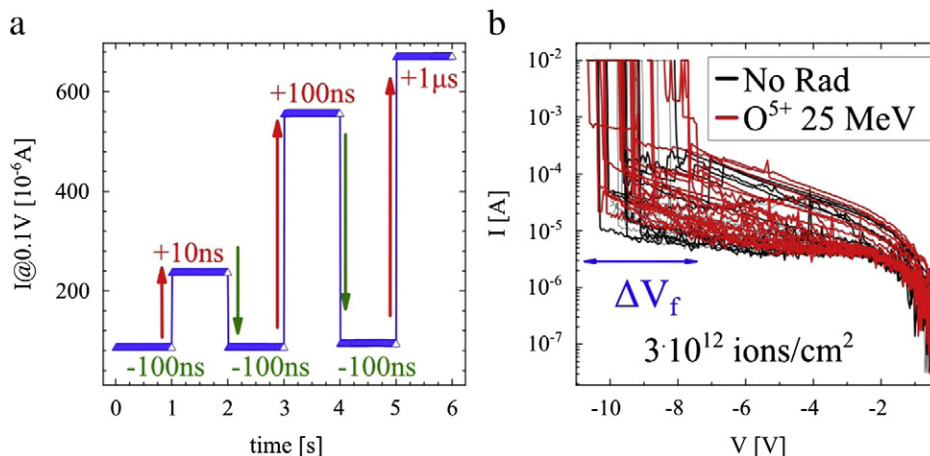

Fig. 6. (a) Evolution of the conductivity when applying nanosecond voltage pulses. (b) Radiation hardness analysis of TiO$_2$ memory devices irradiated with oxygen ions at 25 MeV. The dose was 10^{12} ions/cm^2.

Fig. 6(b) depicts electroforming runs of these 200 devices in semi-log scale. Neither the threshold value for initialization, nor the leakage current before electroforming ($V < V_f$) presents significant changes upon irradiation. Both trends indicate that, at the 10^{12} ions/cm^2 dose level, it is not possible to generate clusters of defects that form early filaments connecting both electrodes in an effective way. The presence of these radiation-induced defects would degrade the RS characteristics.

Additionally, we checked the I–V and HSL curves of randomly sampled devices (data not shown); nevertheless no variation between irradiated and non-irradiated devices was found. This suggests that the amount of defects (*i.e.* oxygen vacancies) after oxygen irradiation is much lower than that produced during the electrical breakdown. The fact that no difference was found after irradiation in the I–V and the HSL curves is consistent with a picture where all the RS characteristics are mainly dictated by the electroforming process.

4. Conclusions

We micro-fabricated crossbar arrays of titanium dioxide using three different electrodes. We characterized the morphology of the devices and tested electrically their memory properties. We obtained a retentivity of 10^5 s, an endurance of 10^4 cycles and switching with time pulse below 10 ns.

Finally, we exposed the devices to 10^{12} ions/cm^2 of 25-MeV O-ion radiation. Oxygen ions did not degrade the $V_{forming}$ of the devices. These results suggest that TiO$_2$-based devices are good candidates for critical components in radiation-hardened electronics.

References

[1] A. Sawa, Mater. Today 11 (2008) 28.
[2] R. Waser, R. Dittmann, G. Staikov, K. Szot, Adv. Mater. 21 (2009) 2632.
[3] J.J. Yang, I.H. Inoue, T. Mikolajick, C.S. Hwang, MRS Bull. 37 (2012) 131.
[4] A.C. Torrezan, J.P. Strachan, G.M. Ribeiro, R.S. Williams, Nanotechnology 22 (2011) 485203.
[5] D. Ielmini, S. Spiga, F. Nardi, C. Cagli, A. Lamperti, E. Cianci, M. Fanciulli, J. Appl. Phys. 109 (2011) 3.
[6] Z. Liu, J. Gan, T. Yew, Appl. Phys. Lett. 100 (2012) 153503.
[7] C. Kugeler, R. Rosezin, R. Weng, R. Waser, S. Menzel, B. Klopstra, U. Bottger, 9th IEEE Conf. on Nanotechnology, 2009, p. 900.
[8] F. Palumbo, E. Miranda, G. Ghibaudo, V. Jousseaume, IEEE Elec. Dev. Lett. 33 (2012) 1057.
[9] S. Long, X. Lian, C. Cagli, X. Cartoixa, E. Miranda, D. Jimenez, L. Perniola, M. Liu, J. Suie, Appl. Phys. Lett. 102 (2013) 183505.
[10] S. Long, X. Lian, T. Ye, C. Cagli, L. Perniola, E. Miranda, M. Liu, J. Sue, IEEE Elec. Dev. Lett. 34 (2013) 623.
[11] K. Fujiwara, T. Nemoto, M.J. Rozenberg, Y. Nakamura, H. Takagi Jpn, J. Appl. Phys. 47 (2008) 6266.
[12] H. Kim, D.W. Kim, Appl. Phys. A 102 (2011) 949.
[13] T.Y. Huang, F.C. Jong, T.S. Chao, H.C. Lin, L.Y. Leu, K. Young, C.H. Lin, K.Y. Chin, IEEE Elec. Dev. Lett. 19 (1998) 256.
[14] Y. Wang, L. Hangbing, W. Wang, Q. Liu, S. Long, W. Wang, H. Zongliang, Z. Sen, L. Yingtao, Z. Qingyun, L. Wentai, Y. Jianhong, M. Liu, IEEE Elec. Dev. Lett. 31 (2010) 1470.
[15] B. Butcher, X. He, M. Huang, Y. Wang, Q. Liu, H. Lv, M. Liu, W. Wang, Nanotechnology 21 (2010) 475206.
[16] H.J. Barnaby, S. Malley, M. Land, S. Charnicki, A. Kathuria, B. Wilkens, E. Deionno, W.M. Tong, IEEE Trans. Nucl. Sci. 58 (2011) 2838.
[17] K. Shibuya, D. Okuyama, R. Kumai, Y. Yamasaki, H. Nakao, Y. Murakami, Y. Taguchi, T. Arima, M. Kawasaki, Y. Tokura, Phys. Rev. B 84 (2011) 165108.
[18] H. Shin, M.R. De Guire, A.H. Heuer, J. Appl. Phys. 83 (1998) 3311.
[19] A.R. Forouhi, I. Bloomer, Phys. Rev. B 34 (1986) 7018.
[20] N.D. Lang, W. Kohn, Phys. Rev. B 3 (1971) 1215.
[21] S. Kim, Y.K. Choi, IEEE Trans. Elec. Dev. 56 (2009) 3049.
[22] N. Ghenzi, M.J. Sanchez, P. Levy, J. Phys. D. Appl. Phys. 46 (2013) 415101.
[23] N. Ghenzi, M.J. Sánchez, F.G. Marlasca, P. Levy, M.J. Rozenberg, J. Appl. Phys. 107 (2010) 93719.
[24] F.G. Marlasca, N. Ghenzi, P. Stoliar, M.J. Sánchez, M.J. Rozenberg, A.G. Leyva, P. Levy, Appl. Phys. Lett. 98 (2011) 123502.
[25] F. Alibart, L. Gao, B. Hoskins, D. Strukov, Nanotechnology 23 (2012) 75201.
[26] P. Stoliar, A.J. Kreiner, M.E. Debray, M.E. Caraballo, A.A. Valda, J. Davidson, M. Davidson, J.M. Kesque, H. Somacal, H. DiPaolo, A.A. Burlon, M.J. Ozafrán, M.E. Vázquez, D. Minsky, E.M. Heber, V.A. Trivillin, A.E. Schwint, Appl. Radiat. Isot. 61 (2004) 771.
[27] G.F. Knoll, in: John Wiley & Sons (Ed.), Radiation Detection and Measurement3rd edition, 2010.
[28] M.G. Bowler, in: Pergamon Press (Ed.), Nuclear Physics, 1973.
[29] J.F. Ziegler, J.P. Biersack, SRIM — The Stopping and Range of Ions in Solids, 1985.
[30] G. Pasquini, P. Levy, L. Civale, G. Nieva, H. Lanza, Phys. C 274 (1997) 165.